Integrated Response Surface Methodology and Gaussian Process Regression for Multi-Objective Particle Swarm Optimization of Tribological Performance in AZ91/ZrO_2 Composites

S. Rajesh*[1], Arul N[2], Prabu L[3], Velmurugan S[4]

[1]*Professor, Department of Research, Meenakshi Academy of Higher Education and Research (MAHER), 12, Vembuliamman Koil Street, West K.K.Nagar, Chennai, Tamil Nadu, India.

[2]Assistant Professor, Department of Mechatronics Engineering, Sona College of Technology, Salem, Tamil Nadu, India.

[3]Associate Professor, Department of Mechanical Engineering, Sri Shanmugha College of Engineering and Technology, Salem, Tamil Nadu, India.

[4]Assistant Professor, Department of Mechanical Engineering, Vel Tech High Tech Dr. Rangarajan Dr. Sakunthala Engineering College, Trivallur, Tamil Nadu, India.

Email ID: [1]*rajeshsudhakar@maher.ac.in, [2]arul88ind@gmail.com, [3]lprabu.cad@gmail.com, [4]ivelu00@gmail.com

Abstract

The tribological performance of magnesium-based metal matrix composites under elevated-temperature sliding conditions is governed by complex interactions among operating parameters and ceramic reinforcement. This investigation examines the dry sliding wear and friction characteristics of AZ91 magnesium alloy reinforced with ZrO_2 particles using Box–Behnken design (BBD), response surface methodology (RSM), Gaussian process regression (GPR), and multi-objective particle swarm optimization (MOPSO). A 29-run BBD framework incorporated four independent variables: temperature (60–200 °C), sliding speed (0.75–1.95 m/s), normal load (15–55 N), and ZrO_2 concentration (1.5–7.5 wt.%). Specific wear rate (SWR) and coefficient of friction (COF) were selected as performance responses. Quadratic RSM models achieved determination coefficients of 0.9985 and 0.9984 for SWR and COF, respectively, while five-fold cross-validation yielded R^2 values of 0.9913 and 0.9882. Corresponding GPR models attained cross-validated R^2 values of 0.9863 and 0.9868, demonstrating close predictive agreement. Multi-objective optimization identified a compromise condition comprising 60°C, 1.9499 m/s sliding speed, 15.00 N normal load, and 4.6901 wt.% ZrO_2, with predicted SWR and COF values of 0.21003×10^{-3} $mm^3/(N \cdot m)$ and 0.29220, respectively. Cross-model verification revealed prediction differences below 1% for both responses at the selected operating conditions. The findings demonstrate the applicability of integrated statistical modelling, machine learning, and Pareto-based optimization for examining wear–friction relationships and identifying favourable parameter combinations within the investigated design domain.

Keywords: Tribology, Sliding wear, Friction, Machine learning, Box-Behnken Design.

1. Introduction

Magnesium alloys have been extensively investigated for lightweight structural applications owing to their favorable strength-to-weight ratio, dimensional stability, and excellent damping characteristics. Previous studies have focused on improving their mechanical, microstructural, and tribological properties through advanced fabrication techniques and material modifications. Recent research has also emphasized experimental design, statistical optimization, and predictive modeling to enhance material performance and processing efficiency. Stir-cast AZ91 magnesium alloy reinforced with 12 wt.% ZrB_2 exhibited uniform particle distribution with minimal casting defects. Taguchi L9, grey relational analysis,

and ANOVA identified applied load as the dominant factor influencing wear rate and coefficient of friction. Minimum wear was obtained at 10 N load, 2 m/s sliding velocity, and 1500 m sliding distance. Dry drilling characteristics of AZ91 magnesium alloy reinforced with 10 wt.% SiC were investigated using CNC machining with CBN-coated drill bits. The Taguchi L16 design and ANOVA-based general linear model (GLM) evaluated spindle speed, feed rate, and drill diameter.

Optimization of stir-casting parameters for AZ91/ZrO_2 magnesium composites was performed using Taguchi L16, ANOVA, and artificial neural networks. Maximum tensile strength of 222 MPa and hardness of 81.68 HV were obtained at 650 °C, 550 rpm, 6 wt.% ZrO_2, and 10 min stirring time. ANOVA identified stirring speed (71%) and melt temperature (19%) as influential factors, R = 0.9966 (Shaban et al., 2026). Minimum quantity lubrication-assisted machining of AZ91 magnesium alloy was investigated using machine learning to predict tool wear and chip characteristics, achieving 34.1% lower MSE and 17.1% lower MAE, indicating improved machining prediction accuracy (Al Bukhari & Pervaiz, 2025). Surface modification of biodegradable magnesium alloy was conducted through micro-electrical discharge milling to investigate machining time and surface roughness. Among Gaussian process regression (GPR), the GPR model demonstrated superior prediction accuracy. Preference-based Marine Predators Algorithm optimization was subsequently employed to identify Pareto-optimal machining parameters (Saha et al., 2025).

Kinetic modeling of Cu/ZnO/Al_2O_3, Cu/ZnO/Al_2O_3/ZrO_2, and Cu/ZnO/ZrO_2 catalysts for CO_2 hydrogenation to methanol was critically examined. The analysis identified inconsistencies in transferring adsorption constants and kinetic parameters between different catalyst systems (Bisotti et al., 2025). Catalytic hydrogenation of CO_2 to methanol was investigated using Cu–ZnO catalysts supported on tetragonal and monoclinic ZrO_2 polymorphs. Operating parameters, including temperature, pressure, gas hourly space velocity, and H_2/CO_2 ratio, were examined in a fixed-bed reactor (Marcos et al., 2022). Response Surface Methodology (RSM) based on central composite design was employed to optimize Ag/ZrO_2 hybrid nanolubricants for improved tribological performance. ZrO_2 incorporation enhanced lubrication characteristics, reducing the coefficient of friction by 23.9% and wear scar diameter by 23.6% (Akkaya & Aksoy, 2026).

Quaternized polyphenylene oxide membranes incorporated with APTES-functionalized ZrO_2 nanoparticles were optimized for anion exchange membrane water electrolysis. Box–Behnken RSM and ANOVA identified optimum conditions of 4.38 wt.% APTES–ZrO_2, 0.625 molar ratio, and 11.32 wt.% QPPO (Choden et al., 2026). Response Surface Methodology (RSM) was employed to evaluate the influence of nano-ZrO_2 reinforcement on the mechanical and water absorption properties of cementitious composites. The quadratic regression model demonstrated strong predictive accuracy (R^2 = 0.9650), while ZrO_2 incorporation improved long-term compressive strength through pore structure refinement (Wu et al., 2026). Micro-EDM of aluminum nitride ceramics was conducted using canola oil methyl ester dielectric containing 0.5 wt.% ZrO_2 nanoparticles. RSM-based Box–Behnken design and ANOVA identified dielectric type as the major factor influencing material removal rate (33.0%), relative wear rate (37.4%), and roughness (45.2%) (Ravi et al., 2026).

High-entropy alloy particle-reinforced AZ91 magnesium composites containing $(AlTi)_{0.5}FeCoCrNi$ were fabricated through wire arc additive manufacturing and friction stir processing. Optimum processing at 500–600 rpm and 40 mm/min improved particle dispersion and interfacial bonding (Sui et al., 2026). Hybrid AZ91D magnesium composites reinforced with Al_2O_3 and TiO_2 nanoparticles were investigated to improve mechanical, tribological, and

corrosion properties. The M3A1T composite containing 3% Al_2O_3 and 1% TiO_2 exhibited refined microstructure, homogeneous particle dispersion, and superior wear resistance (Nagarajan et al., 2026). Powder metallurgy was employed to fabricate AZ91 magnesium composites containing 0.5–2 wt.% nano-TiC and 0.5 wt.% reduced graphene oxide. The hybrid reinforcements improved microhardness by approximately 45.9% relative to the unreinforced alloy. At 1.5 wt.% TiC, wear rate and coefficient of friction decreased by 40.7% and 49.33% (Kumar & Gupta, 2026). A protective Ni/polyaniline/silane tri-layer coating was developed on AZ91 magnesium alloy to enhance corrosion resistance. Surface characterization revealed a porous polyaniline intermediate layer and smooth hydrophobic silane outer layer. Electrochemical testing in 3.5% NaCl showed corrosion resistance increasing from 0.2 to 86.9 kΩ cm^2 (Ali et al., 2026).

The microstructural deformation behavior of coarse-grained AZ91 magnesium alloy was investigated using single-layer, double-layer, and multilayer grain configurations. Microstructural analysis revealed localized plastic deformation in single-layer specimens, while multilayer configurations exhibited improved strain distribution and grain interactions (Wang et al., 2026). Selective laser-melted AZ91 magnesium alloy was modified through combined nanosecond and femtosecond laser shock peening to improve surface integrity. The optimized treatment at 0.6 J and three impacts reduced surface porosity, while surface roughness decreased by 35%, from 10.1 to 6.6 μm (Zhao et al., 2026). Thermal plasma irradiation was applied to AZ91 magnesium alloy for exposure durations of 5–25 min to investigate surface morphology and mechanical properties. SEM revealed the formation of craters, pores, cavities, bumps, and particulates, with their dimensions increasing at longer exposure times (Shoaib et al., 2026).

The novelty of this study lies in integrating Box–Behnken design-based response surface methodology (RSM), Gaussian process regression (GPR), and multi-objective particle swarm optimization (MOPSO) into a unified computational framework for investigating the high-temperature tribological behaviour of AZ91 magnesium alloy reinforced with ZrO_2 particles. Unlike conventional single-model optimization approaches, the framework incorporates comparative predictive assessment through five-fold cross-validation, Pareto-based simultaneous minimization of specific wear rate and coefficient of friction, and cross-model verification of optimized operating conditions. This integrated strategy provides a systematic approach for evaluating nonlinear parameter interactions, assessing surrogate-model agreement, and identifying favourable wear–friction compromises within the investigated design space.

2. Materials and methods

2.1. Materials and preparation of AZ91/ZrO_2 composites

AZ91 magnesium alloy selected as metallic matrix, while zirconium dioxide (ZrO_2) particles were considered as ceramic reinforcement to investigate the influence of particulate incorporation on elevated-temperature tribological behaviour. The reinforcement concentrations were defined between 1.5 and 7.5 wt.%, with 4.5 wt.% representing the central composition. The matrix–reinforcement combinations were established to examine the combined influence of ceramic loading and sliding conditions on SWR and COF.

Stir casting was selected as the fabrication route for the composite specimens. The intended processing sequence comprises melting the AZ91 matrix under a suitable protective

atmosphere, preheating the ceramic particles, introducing the reinforcement into the melt under controlled agitation, and transferring the mixture into prepared moulds.

2.2. High-temperature tribological testing

Dry sliding performance was assessed computationally for a pin-on-disc tribological configuration, with temperature, sliding velocity, applied normal force and ZrO_2 concentration treated as independent variables. The investigated ranges were 60–200 °C, 0.75–1.95 m/s, 15–55 N and 1.5–7.5 wt.%, respectively. SWR and COF were selected as the principal response variables for evaluating material loss and interfacial friction.

For physical testing, SWR can be determined from specimen mass loss, density, applied load and total sliding distance. The volume removed during contact is expressed as:

$$\Delta V = [(m_i - m_f)/\rho] \times 1000 \quad (1)$$

where ΔV denotes wear volume in mm^3, m_i and m_f represent initial and final specimen masses in grams, respectively, and ρ is the composite density in g/cm^3.

The specific wear rate is calculated using:

$$SWR = \Delta V/(F_n \times L) \quad (2)$$

where F_n is the normal load in newtons and L represents the accumulated sliding distance in metres. The coefficient of friction is defined as: (Yamaguchi et al., 2027).

$$COF = F_f/F_n \quad (3)$$

where F_f corresponds to the tangential frictional force. The equations provide the measurement framework for subsequent physical validation.

2.3. Box–Behnken experimental design

Four-factor, three-level Box–Behnken design (BBD) were employed to establish computational investigation matrix (Singh et al., 2026). Design comprised 29 combinations, including five centre-point entries, enabling evaluation of individual factor contributions, quadratic effects and two-factor interactions. Temperature (A), sliding speed (B), normal load (C) and ZrO_2 concentration (D) were selected as independent variables, while SWR and COF constituted the two dependent responses.

Table 1. Independent variables and levels adopted for BBD framework.

Factor	Variable	Unit	Low (−1)	Centre (0)	High (+1)
A	Temperature	°C	60	130	200
B	Sliding speed	m/s	0.75	1.35	1.95
C	Normal load	N	15	35	55
D	ZrO_2 concentration	wt.%	1.5	4.5	7.5

The coded value of each factor was obtained from:

$$x_i = (X_i - X_0)/\Delta X_i \quad (4)$$

where X_i denotes the actual factor setting, X_0 represents its central value and ΔX_i corresponds to half the investigated range. The response matrix was used for subsequent quadratic regression and machine-learning analysis.

2.4. RSM methodology

Response surface methodology (RSM) applied to establish mathematical relationships between four input factors and the selected tribological responses. Separate second-order polynomial models were fitted for SWR and COF to describe linear contributions, pairwise interactions and curvature across the investigated domain. The general quadratic equation is expressed as:

$$Y = \beta_0 + \Sigma\beta_i x_i + \Sigma\beta_{ii} x_i^2 + \Sigma\Sigma\beta_{ij} x_i x_j + \varepsilon \quad (5)$$

where Y represents the modelled response, β_0 denotes the intercept, β_i represents linear coefficients, β_{ii} indicates quadratic coefficients, β_{ij} corresponds to interaction coefficients and ε denotes the residual error.

ANOVA were incorporated to evaluate significance of model terms and overall regression adequacy. Model assessment included the coefficient of determination, adjusted and predicted determination coefficients, F-statistics, probability values, lack-of-fit assessment and residual diagnostics. Three-dimensional response surfaces and contour diagrams were used to examine interactions between selected factors while maintaining the remaining variables at specified settings. Numerical desirability optimization was employed to identify operating conditions associated with simultaneous minimization of SWR and COF.

2.5. Gaussian process regression modelling

Gaussian process regression (GPR) was implemented in MATLAB to represent nonlinear relationships between the four operating variables and the tribological responses. Independent regression models were established for SWR and COF using temperature, sliding speed, normal load and ZrO_2 concentration as predictor variables. Automatic relevance determination Matérn 5/2 covariance function was selected with basis function and standardized predictors.

The GPR framework expresses the response as:

$$Y(x) = f(x) + \varepsilon \quad (6)$$

where f(x) represents a Gaussian process and ε denotes observational noise. The covariance relationship between two input vectors is described through the Matérn 5/2 kernel:

$$k(x,x') = \sigma_f^2(1 + \sqrt{5}r + 5r^2/3)\exp(-\sqrt{5}r) \quad (7)$$

$$r = \sqrt{[\Sigma((x_j - x'_j)^2/\ell_j^2)]} \quad (8)$$

where σ_f^2 represents signal variance and ℓ_j denotes characteristic length scale by each predictor.

Five-fold cross-validation were adopted to examine predictive performance. Identical data partitions were used for RSM and GPR to maintain consistency in model comparison.

Predictive accuracy were evaluated through R^2, mean absolute error (MAE) and root mean square error (RMSE):

$$R^2 = 1 - [\Sigma(y_i - \hat{y}_i)^2/\Sigma(y_i - \bar{y})^2] \quad (9)$$

$$RMSE = \sqrt{[(1/n)\Sigma(y_i - \hat{y}_i)^2]} \quad (10)$$

$$MAE = (1/n)\Sigma|y_i - \hat{y}_i| \quad (11)$$

where y_i denotes reference response, $\hat{y}_i$ represents the predicted response, $\bar{y}$ were mean reference response and n indicates number of observations.

2.6. Multi-objective particle swarm optimization

Multi-objective particle swarm optimization were coupled with the fitted GPR models to investigate operating conditions that minimize SWR and COF simultaneously. The optimization employed a population of 60 particles, 200 iterations and an external archive capacity of 100 nondominated solutions. Candidate positions were constrained within the original four-factor design boundaries.

The optimization objectives were formulated as:

$$\text{Minimize } f_1(x) = SWR_GPR(x) \quad (12)$$

$$\text{Minimize } f_2(x) = COF_GPR(x) \quad (13)$$

subject to:

$$60 \leq T \leq 200\ ^\circ C$$

$$0.75 \leq V_s \leq 1.95\ m/s$$

$$15 \leq F_n \leq 55\ N$$

$$1.5 \leq ZrO_2 \leq 7.5\ wt.\%$$

Particle movement was governed by velocity and position updates:

$$v_i(t+1) = wv_i(t) + c_1r_1[p_i - x_i(t)] + c_2r_2[g_i - x_i(t)] \quad (14)$$

$$x_i(t+1) = x_i(t) + v_i(t+1) \quad (15)$$

where w is the inertia coefficient, c_1 and c_2 were acceleration constants, r_1 and r_2 shows random values, p_i denotes personal-best position and g_i represents a selected archive leader.

Nondominated solutions were retained within the external repository to describe the trade-off between the two objectives. A normalized compromise-selection procedure was applied to identify a balanced operating condition from the resulting Pareto front. Optimization behaviour was examined through objective convergence and Pareto-distribution plots.

2.7. Cross-model optimization verification

The optimized conditions obtained through RSM desirability analysis and GPR-assisted MOPSO were evaluated using both fitted regression approaches. For each operating condition, SWR and COF predictions were generated independently from the quadratic RSM equations and the GPR surrogate models. This comparison was intended to assess agreement between the modelling frameworks and identify differences associated with the selected optimization strategies.

Relative prediction disagreement was determined as:

$$\text{Disagreement (\%)} = |Y_GPR - Y_RSM|/|Y_RSM| \times 100 \quad (16)$$

where Y_GPR and Y_RSM denote the corresponding model predictions at identical input settings. The comparison provides an internal verification of surrogate-model consistency without constituting independent experimental validation.

2.8. Confirmation and statistical assessment

A separate confirmation framework was established for the two optimized parameter combinations. SWR and COF were considered individually, and each confirmation condition was represented by a mean response and standard deviation. Prediction deviations were evaluated relative to the corresponding RSM and GPR estimates using:

$$\text{Prediction error (\%)} = |Y_{confirm} - Y_{predict}|/|Y_{confirm}| \times 100 \quad (17)$$

where $Y_{confirm}$ represents the confirmation response and $Y_{predict}$ denotes the corresponding model estimate.

3. Results and discussion

3.1. Tribological response characteristics

The influence of temperature, sliding speed, normal load, and ZrO_2 reinforcement on the tribological responses of AZ91 magnesium alloy composites was examined using a 29-run Box–Behnken design. SWR and COF was evaluated across the investigated parameter combinations. The response matrix covered temperatures of 60–200 °C, sliding speeds of 0.75–1.95 m/s, normal loads of 15–55 N, and reinforcement concentrations of 1.5–7.5 wt.%. Variations in the response values indicated that wear and friction were affected by both individual operating parameters and their combined interactions. Quadratic regression and Gaussian process regression were subsequently employed to characterize these relationships and support multi-objective optimization. In earlier research, AZ91 magnesium alloy was coated with $(AlCu)_{3.5}CoCrNiMo/Al_4Ni$ gradient high-entropy alloy using laser cladding to enhance tribological performance. The coating achieved a microhardness of 849.64 $HV_{0.2}$, approximately 9.93 times higher than the substrate, with wear resistance improving by 4.68–13.70 times across room temperature to 200 °C. The lowest coefficient of friction (0.3911) was recorded at 200 °C (Hu et al., 2026).

Table 2. BBD response matrix for AZ91/ZrO_2 composites.

Run	Temperature (°C)	Speed (m/s)	Load (N)	ZrO_2 (wt.%)	SWR ($\times 10^{-3}$ $mm^3/N{\cdot}m$)	COF

1	60	0.75	35	4.5	0.318	0.368
2	200	0.75	35	4.5	0.436	0.472
3	60	1.95	35	4.5	0.26	0.314
4	200	1.95	35	4.5	0.397	0.426
5	130	1.35	15	1.5	0.343	0.334
6	130	1.35	55	1.5	0.462	0.411
7	130	1.35	15	7.5	0.236	0.367
8	130	1.35	55	7.5	0.359	0.446
9	60	1.35	35	1.5	0.337	0.324
10	200	1.35	35	1.5	0.475	0.433
11	60	1.35	35	7.5	0.238	0.361
12	200	1.35	35	7.5	0.36	0.466
13	130	0.75	15	4.5	0.298	0.377
14	130	1.95	15	4.5	0.262	0.332
15	130	0.75	55	4.5	0.428	0.461
16	130	1.95	55	4.5	0.374	0.403
17	60	1.35	15	4.5	0.226	0.305
18	200	1.35	15	4.5	0.367	0.415
19	60	1.35	55	4.5	0.36	0.386
20	200	1.35	55	4.5	0.482	0.502
21	130	0.75	35	1.5	0.417	0.396
22	130	1.95	35	1.5	0.381	0.347
23	130	0.75	35	7.5	0.313	0.428
24	130	1.95	35	7.5	0.259	0.378
25	130	1.35	35	4.5	0.319	0.37
26	130	1.35	35	4.5	0.315	0.364
27	130	1.35	35	4.5	0.312	0.369
28	130	1.35	35	4.5	0.311	0.369
29	130	1.35	35	4.5	0.313	0.37

3.2. RSM model adequacy and ANOVA

Quadratic response surface models were fitted independently for SWR and COF. The ANOVA results demonstrated statistically significant regression relationships for both responses, with model F-values of 684.15 and 624.72, respectively, and probability values below 0.0001. The coefficients of determination were 0.9985 for SWR and 0.9984 for COF, indicating close agreement between the fitted quadratic functions and the response matrix. Adjusted R^2 values of 0.9971 and 0.9968 further supported the model fits, while predicted R^2 values of 0.9928 and 0.9923 indicated favourable internal predictive consistency.

The lack-of-fit tests were nonsignificant for SWR ($p = 0.3225$) and COF ($p = 0.4119$). The coefficients of variation were 1.13% and 0.72%, respectively. Temperature, sliding speed, normal load, and ZrO_2 concentration were significant contributors to both responses. For SWR, the AB, AC, BC, and BD interaction terms were significant, whereas the BC interaction was particularly important for COF. Quadratic contributions were also significant, confirming the need to account for curvature within the investigated factor ranges. In earlier investigation, AZ31, AZ61, and AZ91 magnesium alloys were subjected to dry bandsaw cutting at 19–50

m/min with a constant feed rate of 1 mm/s to evaluate energy consumption and carbon emissions. ANOVA identified cutting speed as the dominant factor (80% contribution), followed by alloy type (20%), while RSM achieved $R^2 = 0.9821$. Specific energy consumption ranged from 11.244 to 17.378 J/mm³ (Özdamar, 2026).

Table 3. Summary of quadratic RSM model adequacy.

Statistical parameter	SWR	COF
Model F-value	684.15	624.72
Model p-value	<0.0001	<0.0001
R^2	0.9985	0.9984
Predicted R^2	0.9928	0.9923
Adjusted R^2	0.9971	0.9968
Coefficient of variation (%)	1.13	0.72
Lack-of-fit p-value	0.3225	0.4119

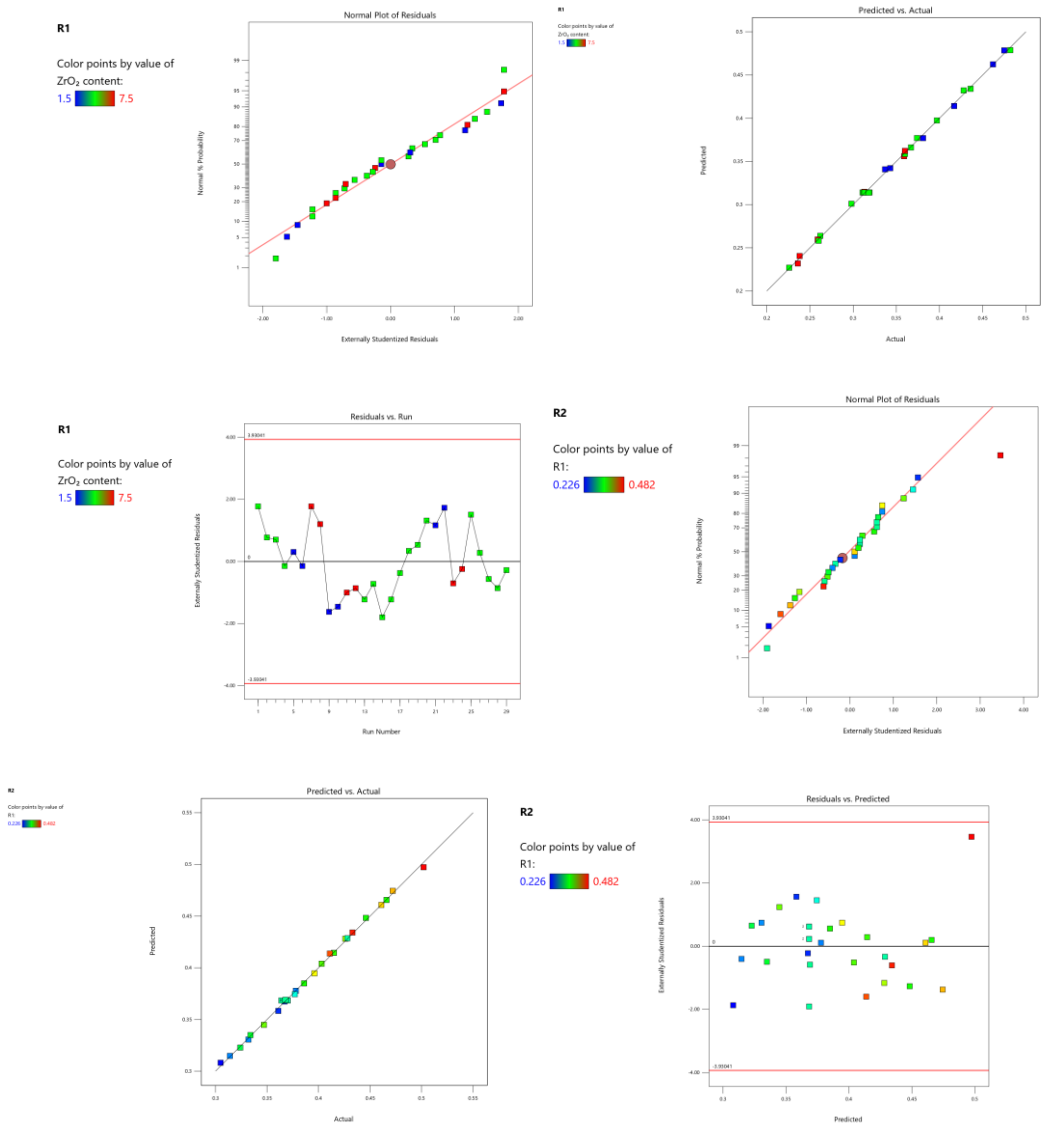

Fig. 1. RSM diagnostic plots for (a) SWR and (b) COF, including normal residual probability, predicted-versus-reference responses, and residual distribution.

3.3. Influence of operating parameters

3.3.1. Temperature

Temperature exhibited a positive influence on SWR and COF across much of the investigated domain. Higher thermal conditions were associated with increased model-estimated material removal and frictional resistance. This tendency may be consistent with temperature-dependent changes in matrix deformation and interfacial contact; however, confirmation of the underlying mechanisms requires physical characterization. The response surfaces also revealed curvature and interactions with sliding speed and normal load, indicating that temperature effects cannot be interpreted independently of the remaining operating conditions.

3.3.2. Sliding speed

Increasing sliding speed generally reduced the estimated SWR and COF within the examined parameter combinations. The extent of this reduction varied with temperature and applied load, reflecting the interaction terms identified through ANOVA. The modelled trends indicate that sliding velocity contributes to the balance between frictional resistance and material removal, although the corresponding surface processes cannot be established from response values alone.

3.3.3. Normal load

Normal load strongly influenced the two tribological responses. Higher applied forces were generally associated with increased SWR and COF, particularly under elevated-temperature conditions. The combined temperature–load and speed–load relationships indicated that the response to mechanical loading depended on the surrounding operating conditions. These observations demonstrate the importance of considering coupled thermal and mechanical effects during parameter selection.

3.3.4. ZrO_2 concentration

Reinforcement concentration significantly affected the predicted tribological behaviour. Increasing ZrO_2 content generally reduced SWR, while its influence on COF differed because the two responses exhibited distinct compositional sensitivities. The nonlinear response patterns indicated that selecting the highest reinforcement concentration did not necessarily provide the most favourable combined wear–friction performance. Intermediate reinforcement levels therefore remained relevant to the multi-objective optimization analysis. In previous study, Low-density polyethylene (LDPE) dispersed in ethylene glycol was subjected to catalytic steam reforming using a 20 wt.% Ni–Co/Al_2O_3–ZrO_2 catalyst for hydrogen production. Optimized operating conditions of 500 °C, steam-to-carbon ratio of 9, and GHSV of 810 h^{-1} achieved 95% feed conversion, 92.72% hydrogen yield, and 97.6% selectivity. The catalyst exhibited a 136 m^2 g^{-1} surface area and improved hydrogen yield by 5–10% (Kalantre & Yadav, 2026).

3.4. RSM response surface analysis

Three-dimensional response surfaces were examined to evaluate interactions among the four independent variables. For SWR, temperature–speed, temperature–load, speed–load, and speed–reinforcement interactions were statistically significant. The surfaces indicated that favourable wear conditions were generally associated with reduced temperature and normal

load, together with suitable sliding speed and reinforcement concentration. For COF, the interaction between sliding speed and normal load was particularly influential.

The curved response profiles demonstrated that the relationships between processing variables and tribological responses were not adequately represented by linear trends alone. Consequently, the quadratic RSM framework provided a suitable mathematical basis for examining the investigated design region and identifying favourable parameter combinations.

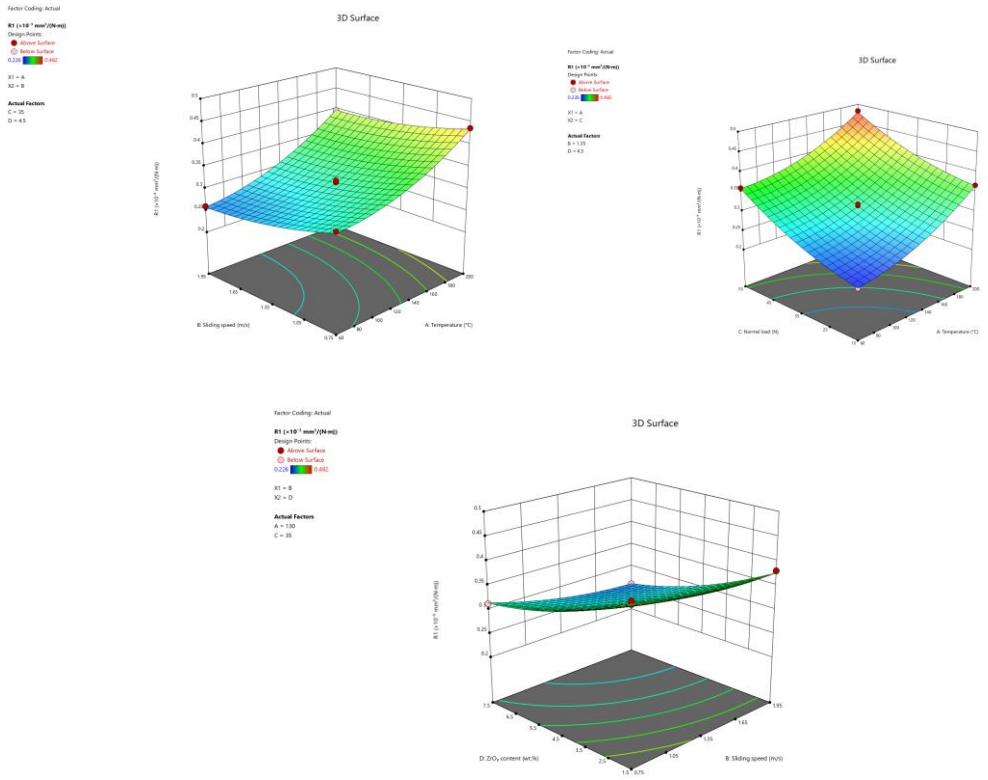

Fig. 2. Quadratic RSM response surfaces illustrating the combined effects of (a) temperature and sliding speed, (b) temperature and normal load, and (c) sliding speed and ZrO_2 concentration on SWR.

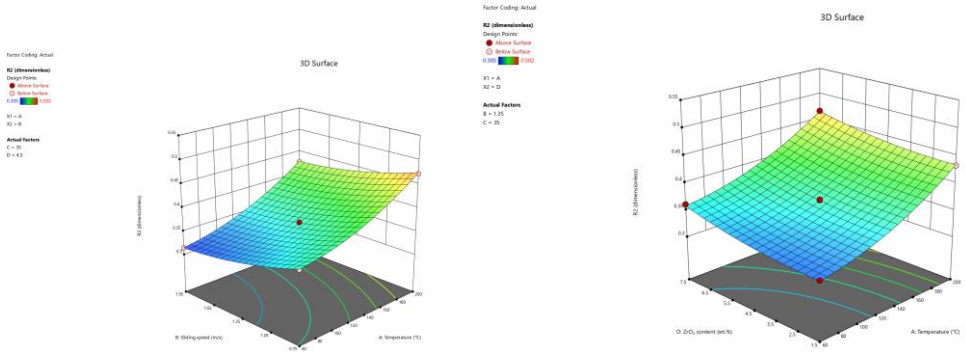

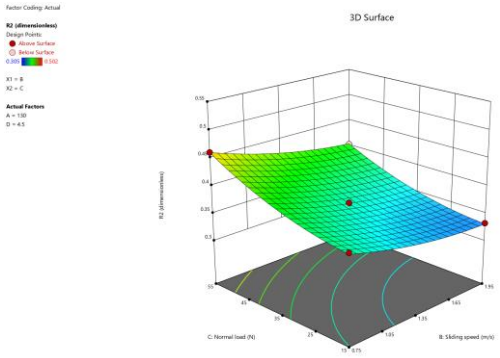

Fig. 3. Quadratic RSM response surfaces for COF: (a) temperature–speed, (b) temperature–load, (c) temperature–ZrO_2, (d) speed–load, (e) speed–ZrO_2, and (f) load–ZrO_2.

3.5. GPR predictive performance

Gaussian process regression models were developed separately for SWR and COF using the four operating variables as predictors. Model performance was evaluated through five-fold cross-validation, allowing predictive assessment using observations excluded from the corresponding training folds. The GPR models attained R^2 values of 0.9863 and 0.9868 for SWR and COF, respectively. The corresponding RMSE values were 0.008236 and 0.005618, while MAE values were 0.006691 and 0.004598.

Predicted-versus-reference plots showed close correspondence between the cross-validated estimates and response values. Residual plots indicated comparatively small prediction deviations across the examined observations. These results support the use of GPR as a nonlinear surrogate within the specified parameter domain, although the limited dataset does not establish predictive reliability outside the investigated ranges. In previous investigation, AZ91 magnesium alloy reinforced with B_4C and graphene nanoplatelets (GNPs) was fabricated through stir casting to investigate wear behavior. Gaussian process regression (GPR) and other machine learning models were employed to predict wear rate, with optimum conditions of 4 wt.% reinforcement, 15 N load, 3 m/s velocity, and 500 m sliding distance. Polynomial regression outperformed GPR and other models, achieving $R^2 = 0.953$, MSE = 0.011, and RMSE = 0.103 (Ammisetti et al., 2024).

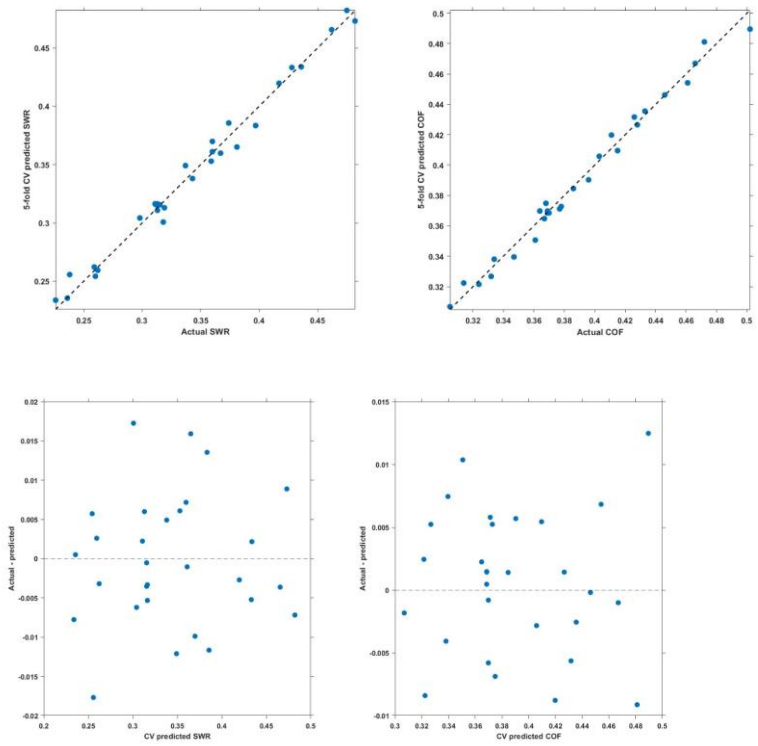

Fig. 4. Five-fold cross-validation performance of GPR: (a) SWR parity plot, (b) COF parity plot, (c) SWR residuals, and (d) COF residuals.

3.6. RSM and GPR model comparison

Both modelling approaches were evaluated using identical five-fold cross-validation partitions. Quadratic RSM achieved R^2 values of 0.9913 for SWR and 0.9882 for COF, compared with 0.9863 and 0.9868 for GPR. RSM also exhibited lower RMSE and MAE for both responses. These findings indicate a modest predictive advantage for the quadratic regression approach within the available response matrix.

Nevertheless, GPR provided a complementary nonlinear representation suitable for exploring the continuous design domain. The close predictive performance of the two models supported their use in cross-model optimization assessment.

Table 4. Five-fold cross-validation comparison of RSM and GPR.

Model	SWR R^2	SWR RMSE	SWR MAE	COF R^2	COF RMSE	COF MAE
Quadratic RSM	0.99133	0.006551	0.005538	0.98820	0.005310	0.004386
GPR	0.98629	0.008236	0.006691	0.98679	0.005618	0.004598

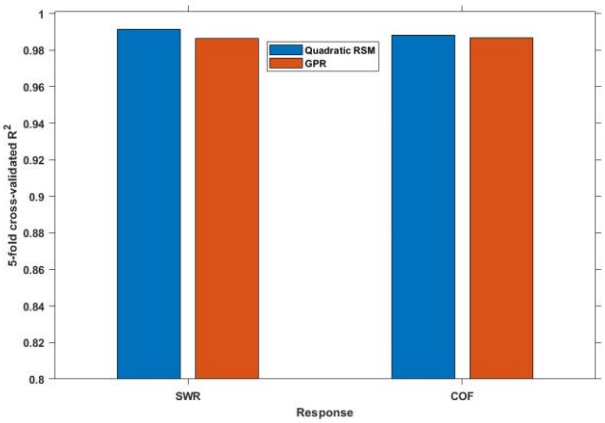

Fig. 5. Comparison of RSM and GPR cross-validation performance for SWR and COF.

3.7. RSM desirability optimization

Numerical desirability analysis was applied to minimize SWR and COF simultaneously. The selected RSM condition corresponded to 62.3564 °C, 1.64557 m/s sliding speed, 20.9772 N normal load, and 4.7907 wt.% ZrO_2. The associated model predictions were 0.223701×10^{-3} mm³/(N·m) for SWR and 0.304777 for COF.

The desirability function reached 1.000 under the specified response limits. This value indicates satisfaction of the defined desirability criteria rather than proof of a unique global optimum. The numerical solution was therefore retained as a reference condition for comparison with the GPR-assisted multi-objective search. In earlier work, Si_3N_4–ZrO_2 composites reinforced with 5% graphene were machined using electrochemical discharge machining (ECDM) with ZnO/TiO_2 nanoparticles and NaOH/KOH electrolytes. Response surface methodology (RSM) based on Box–Behnken design (BBD) was employed to optimize 234 experimental runs, achieving a material removal rate of 0.926 mm³/min (CHINNADURAI et al., 2026).

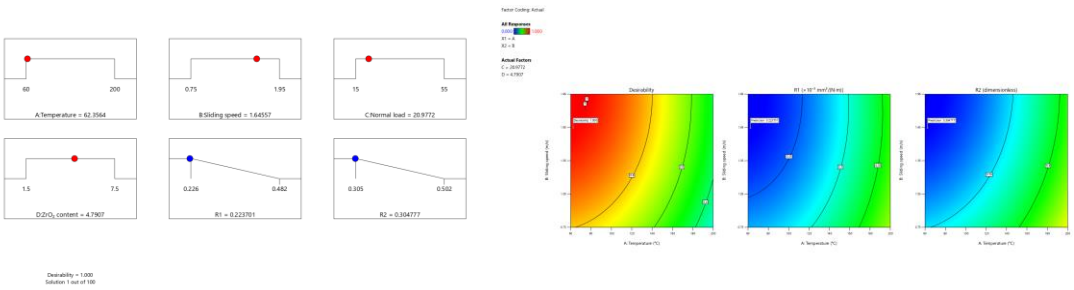

Fig. 6. RSM desirability optimization: (a) parameter ramp and (b) combined desirability contours.

3.8. GPR–MOPSO optimization

The GPR models were integrated with MOPSO to minimize SWR and COF within the four-factor design space. The optimization employed 60 particles over 200 iterations, with an external archive containing up to 100 nondominated solutions. The resulting Pareto front represented alternative compromises between material removal and frictional resistance. The selected normalized compromise condition comprised 60.0021 °C, 1.9499 m/s sliding speed,

15.0017 N normal load, and 4.6901 wt.% ZrO_2. The corresponding GPR estimates were 0.210026×10^{-3} mm³/(N·m) for SWR and 0.292196 for COF. The selected temperature, sliding speed, and normal load were close to the imposed search boundaries, highlighting the importance of restricting interpretation to the investigated design region. The convergence profiles indicated stabilization of the individual objective minima during the optimization process. The Pareto distribution provided additional flexibility for selecting operating conditions according to the relative importance assigned to wear resistance and friction reduction.

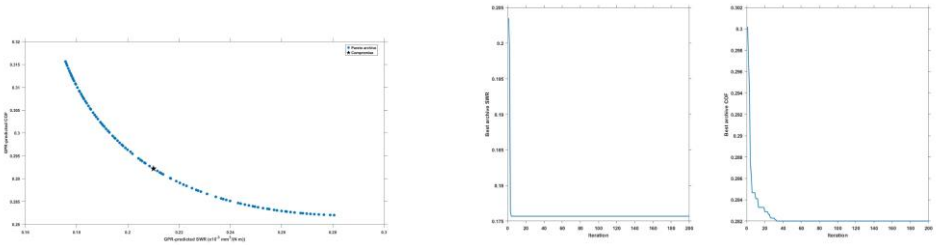

Fig. 7. GPR–MOPSO optimization: (a) Pareto front with selected compromise solution and (b–c) objective convergence profiles.

3.9. Cross-model optimization verification

The RSM and GPR models were used to predict both tribological responses at the two optimized operating conditions. At the RSM optimum, predicted SWR values were 0.22370 and 0.22335 for RSM and GPR, respectively, while the corresponding COF values were 0.30478 and 0.30364. At the GPR–MOPSO condition, the two models estimated SWR values of 0.21154 and 0.21003, together with COF values of 0.29504 and 0.29220.

Prediction disagreement remained below 1% for both responses at each selected condition. In earlier work, AZ91 magnesium alloy reinforced with 23 vol.%. Response surface methodology (RSM) using a face-centered composite design optimized mechanical and wear properties under 20–300 °C and 1–5 N loading conditions. The optimized results achieved 253 MPa compressive strength, 193 MPa yield strength, 0.066 cm³ volume loss, and 840 cm³/m wear rate (Ataya et al., 2025).

Table 5. Cross-model predictions at optimized conditions.

Condition	RSM SWR	GPR SWR	RSM COF	GPR COF
RSM optimum	0.22370	0.22335	0.30478	0.30364
GPR–MOPSO optimum	0.21154	0.21003	0.29504	0.29220

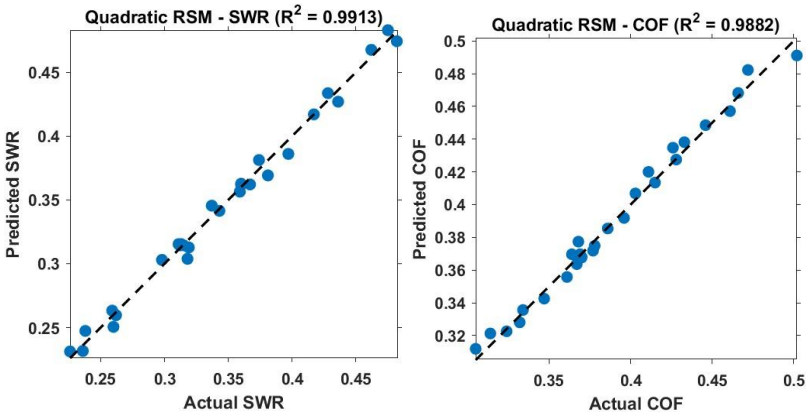

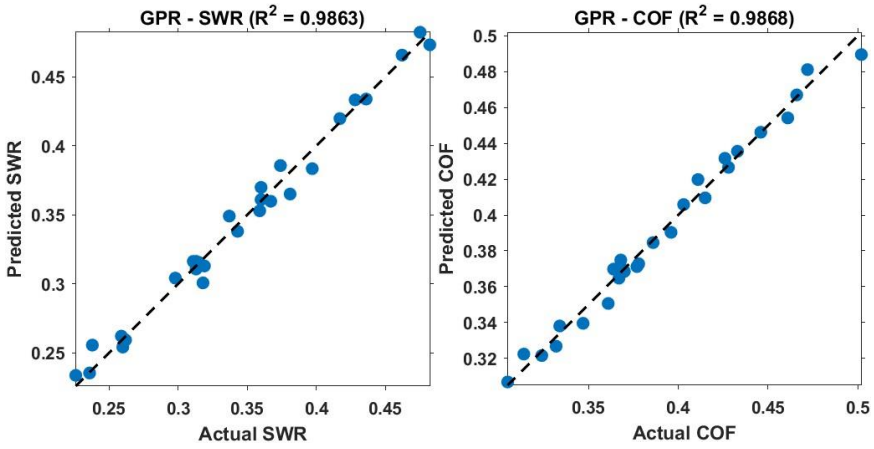

Fig. 8. Cross-model comparison of SWR and COF predictions at the RSM and GPR–MOPSO operating conditions.

3.10. Confirmation analysis

The confirmation dataset was evaluated at the two selected operating conditions to examine agreement with the corresponding model predictions. For the RSM optimum, the confirmation responses were 0.22460 ± 0.00310 × 10^{-3} $mm^3/(N·m)$ for SWR and 0.30610 ± 0.00420 for COF. At the GPR–MOPSO condition, the corresponding values were 0.21280 ± 0.00280 × 10^{-3} $mm^3/(N·m)$ and 0.29410 ± 0.00360.

The confirmation means remained close to the model estimates. However, these values represent a computational confirmation exercise rather than independent physical wear-test measurements.

Table 6. Confirmation responses and model predictions.

Condition	Response	RSM prediction	GPR prediction	Confirmation mean ± SD
RSM optimum	SWR	0.22370	0.22335	0.22460 ± 0.00310
RSM optimum	COF	0.30478	0.30364	0.30610 ± 0.00420
GPR–MOPSO optimum	SWR	0.21154	0.21003	0.21280 ± 0.00280
GPR–MOPSO optimum	COF	0.29504	0.29220	0.29410 ± 0.00360

3.11. Overall discussion

The combined RSM–GPR–MOPSO analysis demonstrated that the investigated tribological responses were sensitive to operating temperature, sliding velocity, normal load, and ceramic reinforcement concentration. Quadratic RSM provided slightly better cross-validated accuracy than GPR, while the GPR-assisted MOPSO framework enabled simultaneous exploration of competing wear and friction objectives. Both surrogate models produced closely aligned predictions at the selected optimization conditions.

3.12. Worn surface morphology and frictional behaviour

Figure 9(a–d) presents the SEM micrographs of the worn surfaces of AZ91 magnesium alloy/ZrO_2 composites at different magnifications. Figure 9(a) reveals numerous parallel grooves and elongated sliding marks along the wear direction, indicating the occurrence of abrasive wear caused by repeated contact between the sliding surfaces. The comparatively

continuous grooves and limited visible surface damage suggest relatively stable material removal. Figure 9(b) exhibits pronounced wear tracks accompanied by fine surface scratches and scattered wear debris, suggesting localized microploughing and abrasive interactions. Figure 9(c) shows comparatively smoother worn regions with shallow grooves and fewer prominent surface irregularities, indicating reduced surface damage and potentially improved wear resistance. In contrast, Figure 9(d) displays deeper grooves, localized surface deformation, adhered debris, and discontinuous surface features, suggesting more severe abrasive wear with possible adhesive contributions. The observed morphological differences indicate that sliding conditions and ZrO_2 reinforcement may influence surface deformation and material removal in AZ91 magnesium alloy composites. Overall, abrasive wear appears to be the predominant wear mechanism, while localized plastic deformation, debris accumulation, and possible adhesive interactions contribute to the observed surface deterioration. However, direct correlation with temperature, sliding speed, normal load, and reinforcement concentration requires the corresponding experimental conditions for each micrograph.In earlier research, Surface morphology of SLM-fabricated AZ91 magnesium alloy revealed reduced surface pores and defects following laser shock peening, although severe plastic deformation increased surface roughness. Combined nanosecond–femtosecond laser treatment reduced surface roughness by 35% (10.1 to 6.6 μm) and refined the average grain size to 5.07 μm, representing a 49.3% reduction (Zhao et al., 2026).

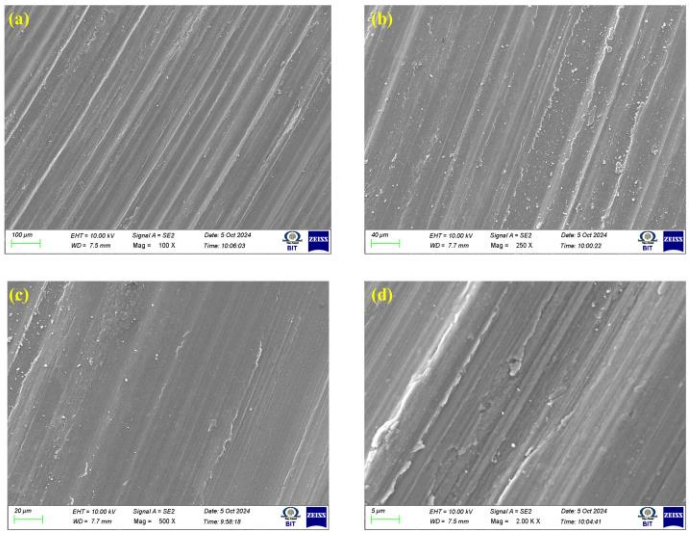

Fig. 9. Comparative wear morphology of AZ91/ZrO_2 composites under selected temperature, sliding speed, and loading conditions.

4. Conclusions

This study investigated the tribological response of AZ91 magnesium alloy reinforced with ZrO_2 particles through an integrated BBD, RSM, GPR, and MOPSO framework. Effects of temperature, sliding speed, normal load, and reinforcement concentration on SWR and COF was examined. The principal findings are summarized below,

a) Temperature and normal load were significant factors influencing both tribological responses. Increasing these parameters generally increased SWR and COF, whereas higher sliding speeds were associated with reduced response values within the investigated design domain.

b) ZrO_2 concentration substantially influenced wear resistance, with increasing reinforcement content generally reducing SWR. However, its effect on COF differed, indicating that reinforcement selection should consider both tribological responses rather than wear resistance alone.

c) Quadratic RSM models exhibited strong fitting performance, achieving R^2 values of 0.9985 for SWR and 0.9984 for COF. The corresponding predicted R^2 values were 0.9928 and 0.9923, supporting the adequacy of the fitted regression relationships.

d) Five-fold cross-validation demonstrated reliable internal predictive performance for both approaches. RSM achieved R^2 values of 0.9913 and 0.9882 for SWR and COF, respectively, while GPR attained 0.9863 and 0.9868. The quadratic models exhibited slightly better predictive accuracy within the available dataset.

e) RSM desirability analysis identified a favourable condition at 62.3564 °C, 1.64557 m/s, 20.9772 N, and 4.7907 wt.% ZrO_2. The corresponding SWR and COF predictions were 0.223701×10^{-3} mm³/(N·m) and 0.304777, respectively.

f) GPR-assisted MOPSO identified a normalized compromise at 60.0021 °C, 1.9499 m/s, 15.0017 N, and 4.6901 wt.% ZrO_2, with predicted SWR and COF values of 0.210026×10^{-3} mm³/(N·m) and 0.292196. Cross-model prediction differences remained below 1% at the selected operating conditions.

Overall, the integrated modelling and optimization framework demonstrated its potential for examining nonlinear wear–friction relationships and identifying favourable operating conditions for AZ91/ZrO_2 composites.

References

Akkaya, M., & Aksoy, A. B. (2026). Synergistic thermal enhancement of Ag/h-BN and Ag/ZrO2 binary hybrid nanolubricants: Central composite design optimization. *Thermochimica Acta*, *763*. https://doi.org/10.1016/j.tca.2026.180400

Al Bukhari, S., & Pervaiz, S. (2025). Advanced Machine Learning Approaches for Predicting Machining Performance in Orthogonal Cutting Process. *Lubricants*, *13*(2). https://doi.org/10.3390/lubricants13020083

Ali, A. B. M., Al-Bahrani, M., Rekha, M. M., Ray, S., Chennakesavulu, K., Sharm, R., Matyakubov, B., Sabirov, S., Smerat, A., Shaik, A. S., & Islam, S. (2026). Designing a robust silane/polyaniline/Ni tri-layer coating for superior corrosion resistance of AZ91 magnesium alloy. *Journal of Sol-Gel Science and Technology*, *117*(3). https://doi.org/10.1007/s10971-026-07106-2

Ammisetti, D. K., Chigilipalli, B. K., Gaddala, B., Kottala, R. K., Aepuru, R., Rao, T. S., Praveenkumar, S., & Kumar, R. (2024). Experimental Investigation and Machine Learning Modeling of Tribological Characteristics of AZ31/B4C/GNPs Hybrid Composites. *Crystals*, *14*(12). https://doi.org/10.3390/cryst14121007

Ataya, S., Alrasheedi, N. H., El-Sayed Seleman, M. M., Eid, R. G., Bakkar, A., Ataya, A., & Fouad, R. A. (2025). Response Surface Methodology-Based Optimization of AZ91

Composites Reinforced with Short Carbon Fibers for Enhanced Mechanical and Wear Properties. *Processes*, *13*(6). https://doi.org/10.3390/pr13061697

Bisotti, F., Moioli, E., & Manenti, F. (2025). Screening kinetic models for CO2-to-methanol over CuO–ZnO–ZrO2–Al2O3 (CZZA) and CuO–ZnO–ZrO2 (CZZ): are they consistent with the experimental evidence? A critical review of the existing kinetic models and relevant literature on experimental characterization of copper-based catalysts for CO2-to-methanol process. *Chemical Engineering Journal*, *503*. https://doi.org/10.1016/j.cej.2024.158033

CHINNADURAI, R., SEKAR, T., PRASANTH, P., & VIJAY, M. (2026). PERFORMANCE PREDICTION AND MULTI-RESPONSE OPTIMIZATION OF Si3N4–ZrO2 COMPOSITES BY ECDM USING HYBRID ANN–BWKA and ALMO MODEL. *Surface Review and Letters*. https://doi.org/10.1142/S0218625X26500708

Choden, Y., Kabir, M. M., Tijing, L., Shon, H. K., Kim, S., & Phuntsho, S. (2026). Multi-parameter optimization and design of QPPO/APTES-ZrO_2 nanocomposite anion exchange membranes via response surface methodology. *Process Safety and Environmental Protection*, *218*. https://doi.org/10.1016/j.psep.2026.109469

Hu, N., Shen, J., Hu, S., Sui, Y., & Geng, K. (2026). Design and preparation of (AlCu)3.5CoCrNiMo/Al4Ni gradient functional coating on AZ91 alloy via laser cladding: Toward superior tribological performance. *Materialia*, *49*. https://doi.org/10.1016/j.mtla.2026.102864

Kalantre, J. B., & Yadav, G. D. (2026). Valorization of Plastic Waste into Hydrogen: Ni–Co/Al2O3–ZrO2 Nanocatalyst for Efficient Steam Reforming of Low-Density Polyethylene (LDPE). *Small*, *22*(22). https://doi.org/10.1002/smll.202513744

Kumar, S., & Gupta, R. N. (2026). Investigation of tribo-mechanical performance of nano-TiC/rGO based hybrid magnesium alloy-based metal matrix composites under dry sliding condition. *Proceedings of the Institution of Mechanical Engineers, Part E: Journal of Process Mechanical Engineering*, *240*(4), 4573–4586. https://doi.org/10.1177/09544089241301274

Marcos, F. C. F., Cavalcanti, F. M., Petrolini, D. D., Lin, L., Betancourt, L. E., Senanayake, S. D., Rodriguez, J. A., Assaf, J. M., Giudici, R., & Assaf, E. M. (2022). Effect of operating parameters on H2/CO2 conversion to methanol over Cu-Zn oxide supported on ZrO2 polymorph catalysts: Characterization and kinetics. *Chemical Engineering Journal*, *427*. https://doi.org/10.1016/j.cej.2021.130947

Nagarajan, M., Sengottaiyan, S., Gurijala, C., & Srinivasan, N. (2026). Enhancement of mechanical, tribological, and corrosion properties of AZ91D magnesium alloy hybrid composites reinforced with Al2O3 and TiO2 nanoparticles for high-performance applications. *Ceramics International*, *52*(14), 26867–26887. https://doi.org/10.1016/j.ceramint.2026.04.238

Özdamar, O. (2026). Energy consumption and carbon footprint analysis of AZ31, AZ61 and AZ91 magnesium alloys during bandsaw cutting. *Multidiscipline Modeling in Materials and Structures*, *22*(4), 1044–1066. https://doi.org/10.1108/MMMS-01-2026-0022

Ravi, M., Thangavel, G., Raja, M., Sakthivel, T. G., Ashok, N., & Bhowmik, A. (2026). Intelligent optimization of micro-electrical discharge machining of aluminum nitride ceramics using nano abrasive zirconium oxide-enhanced biodegradable dielectric. *Scientific Reports*, *16*(1). https://doi.org/10.1038/s41598-026-51911-2

Saha, S., Chaurasia, S., Mazarbhuiya, R. M., Swargiary, A., Maity, S. R., Dey, S., & Debnath, K. (2025). Machine learning based optimization of micro-electro discharge milling responses of AZ91 magnesium alloy for biomedical applications. *Engineering Research Express*, *7*(4). https://doi.org/10.1088/2631-8695/ae2c48

Shaban, E. M., Saravanan, A. R., Rajendranrao, V. R., Muthuvel, B., Rajkumar, D. R., & Revathi, S. (2026). Investigating stir casting process parameters for ZrO_2 reinforced magnesium alloy using backpropagation algorithm. *Interactions*, *247*(1). https://doi.org/10.1007/s10751-026-02412-1

Shoaib, M., Ayub, R. M., Bashir, S., & Akram, M. (2026). Thermal Plasma-Induced Surface Structuring of Mg-Alloy for Improvement of Mechanical Properties. *Journal of Materials Engineering and Performance*, *35*(20), 19877–19889. https://doi.org/10.1007/s11665-025-13034-z

Singh, D. P., Mishra, S., & Yadav, S. K. S. (2026). Parametric Study and Optimization of WEDM Process for Sustainable Machining of Hybrid Magnesium Metal Matrix Composites. *Journal of Advanced Manufacturing Systems*, *25*(3), 539–579. https://doi.org/10.1142/S021968672650023X

Sui, Y., Shen, J., Hu, S., & Hu, N. (2026). Fabrication of HEA particle-reinforced AZ91 magnesium matrix composites via WAAM-FSP hybrid process: Microstructural regulation and performance optimization. *Journal of Magnesium and Alloys*, *23*. https://doi.org/10.1016/j.jma.2026.102219

Wang, X., Xia, D., Gupta, M., & Xu, L. (2026). Study on intergranular strain coordination of Mg alloy AZ91 via controlling ratio between grain size and thickness. *Materials Science and Engineering: A*, *974*. https://doi.org/10.1016/j.msea.2026.150848

Wu, F., Wang, J., Hu, H., Dong, S., Wang, C., & Sun, J. (2026). Synergistic Modification of Cement-Based Materials with Nano-ZnO and Nano-ZrO2 Under Carbonation Mixing: A Response Surface Methodology Study. *Sustainability (Switzerland)*, *18*(14). https://doi.org/10.3390/su18147420

Yamaguchi, T., Yoshihara, C., Nishikawa, T., & Nishi, T. (2027). Age-related decline in plantar friction perception is more strongly associated with frictional stimulus range than with plantar tactile sensitivity. *Tribology International*, *227*. https://doi.org/10.1016/j.triboint.2026.112751

Zhao, X., Wang, Z., Jiang, X., Wang, W., Yu, W., Gao, S., Yan, X., Chang, C., & Zheng, H. (2026). Study on the surface integrity of Additively Manufactured AZ91 Mg alloy combined treated by nanosecond and femtosecond laser. *Optics and Laser Technology*, *197*. https://doi.org/10.1016/j.optlastec.2026.114817